Chinese Chemical Letters 33 (2022) 362–367

Contents lists available at ScienceDirect

Chinese Chemical Letters

journal homepage: www.elsevier.com/locate/cclet

A ferric citrate derived Fe-N-C electrocatalyst with stepwise pyrolysis for highly efficient oxygen reduction reaction

Min Zhang[a], Bolong Yang[a], Ting Yang[b,*], Yahui Yang[b,*], Zhonghua Xiang[a,*]

[a] State Key Laboratory of Organic-Inorganic Composites, Beijing University of Chemical Technology, Beijing 100029, China
[b] College of Chemistry and Chemical Engineering, Hunan Normal University, Changsha 410081, China

ARTICLE INFO

Article history:
Received 21 May 2021
Revised 16 June 2021
Accepted 21 June 2021
Available online 30 June 2021

Keywords:
Oxygen reduction reaction
Non-precious metal electrocatalysts
Fuel cell
ZIF-8, NH_3 activation

ABSTRACT

Unremitting and intensive researches about efficient non-precious metal electrocatalysts are necessary for large-scale commercial applications of fuel cells, while iron and nitrogen co-doped carbon (Fe-N-C) materials has become one of the most promising electrocatalysts to replace Pt-based noble metal catalysts. However, the traditional Fe-doped ZIF with rhomb dodecahedron morphology limits the exposure of active sites and the utilization of atoms, even affecting the performance of the catalyst. Herein, a Fe/N co-doped catalyst with a flower-like morphology was prepared using ferric citrate source along with secondary NH_3 heat treatment. The optimal catalyst (termed as $4Fe_{citrate}$-N-C-3) showed distinguished oxygen reduction reaction (ORR) activity with a half-wave potential of 0.8 and 0.9 V (*vs.* RHE) in acid and alkaline media, respectively. In addition, $4Fe_{citrate}$-N-C-3 maintained more than 80% of original activity even after 50,000 s which is superior to the benchmark Pt/C. The strategy of controlling morphology and composition is meaningful for the optimization of non-precious metal electrocatalysts for ORR in fuel cells or metal-air batteries.

Increasing energy demand and environmental pollution makes researchers more committed to developing sustainable, clean and efficient energy [1–3]. Fuel cell with high energy conversion efficiency has attracted worldwide researchers' ongoing attention, which can convert chemicals into electric energy without producing any pollutants [4,5]. However, the sluggish kinetics of ORR requires platinum group metal (PGMs) catalysts to reduce overpotential of the cathode of proton exchange membrane fuel cells (PEMFCs), which makes equipment cost-prohibitive for large-scale commercial application [6,7]. Although the amount of the platinum has been greatly reduced by adjusting the composition and structure of the catalyst, that does not resolve underlying issue [8–10]. The development of low-cost and durable non-precious metal catalysts with outstanding ORR activity to replace PGMs catalyst is of great significance in PEMFCs [11,12].

The zeolitic imidazolate frameworks (ZIF)-derived Fe-N-C materials was considered as one of the most promising alternatives to PGMs catalysts [13–15]. However, due to the regularly rhomboid dodecahedron structure of ZIF-8, the active site of FeN_4 may be wrapped in the carbonized polyhedron structure [16]. Moreover, micropores-dominated structure can be formed *via* Zn ion volatilize during carbonization process, which makes the active site inaccessible and easy to induce electrolyte and pore blockage [17]. Recently, the structure and morphology has been adjusted to facilitate mass transport [18] or increase the exposed active sites for enhancing ORR performance [19,20]. For instance, Wan *et al.* reported an concave Fe-N-C catalyst, which increased external surface area to expose more inaccessible FeN_4 active sites, demonstrating excellent ORR activity and high power density in PEMFCs [21]. Additionally, transition-metal and nitrogen co-doped carbon nanotube composite exhibits an outstanding electrocatalytic activity and stability due to the abundant nitrogen atoms and pore structure [22–24]. Wang *et al.* reported a simple NaCl-assisted method to prepare a high-performance nitrogen-doped electrocatalyst with abundant FeN_4 sites [25]. Therefore, rational structure regulation for the catalyst to generate more exposed active sites is an effective method to develop practical PGM-free catalysts in devices.

Herein, we designed a ferric citrate derived Fe-N-C catalyst with flower-like morphology after secondary heat treatment by NH_3. In the original coordination framework of ZIF-8, partial 2-methylimidazole ligands were replaced and the citrate ion can coordinate with zinc nodes of ZIF-8 due to the strong intercalation between citrate salt and metal ions [26,27]. Such hybrid coordination is conductive to the formation of the flower-like structure

* Corresponding authors.
E-mail addresses: 297902195@qq.com (T. Yang), yangyahui2002@sina.com (Y. Yang), xiangzh@mail.buct.edu.cn (Z. Xiang).

https://doi.org/10.1016/j.cclet.2021.06.054
1001-8417/

and Fe-N coordination, leading to notably increased intrinsic activity with high ORR kinetics [28]. The flower-like morphology can facilitate the explosion of accessible active sites and form mesoporous pore compared with conventional regular polyhedron dodecahedron of ZIF-8, which is conductive to mass transfer in the device [29]. Furthermore, the atomic content of the total N, pyridine N and graphite N were increased by secondary NH_3 heat treatment to improve the ORR activity [30–33]. The prepared catalyst 4Fe$_{citrate}$-N-C-3 exhibited good catalytic activity with a half-wave potential of 0.8 and 0.9 V (*vs.* RHE) in acid and alkaline electrolyte. Additionally, 4Fe$_{citrate}$-N-C-3 owns excellent cycling stability with only 20 mV degradation after 5000 cycles and good resistance to methanol toxicity than the benchmark Pt/C.

All the chemicals used in the synthesis of catalysts were analytical purity and no further purification was made. 2-Methylimidazole (98%) was purchased from Heowns Biochem LLC. Ferric citrate was purchased from Macklin (Shanghai, China). Zinc nitrate hexahydrate ($Zn(NO_3)_2{\cdot}6H_2O$, 98%) was purchased from Aladdin (Shanghai, China). Nafion solution was purchased from Energy Chemical. Commercial Pt/C (20 wt%) was obtained from Alfa Aesar Chemical Co., Ltd. High-purity (99.99%) oxygen gas and nitrogen gas were obtained from Shi yuan Jing ye (Beijing) Air Power Technology Development Co., Ltd. The deionized water was made by the laboratory water purifier (18.3 MΩ cm).

The catalyst we synthesized was labeled as *X*Fe$_y$-N-C-*Z*, where *X* denotes the percentage of iron added moles compared to zinc and *y* is the ferric salt with different anions, *Z* is the molar ratio between 2-methylimidazole and added metal (1, 2, 3 corresponding to the molar ratio between 2-methylimidazole ligand and added metal varies from 1:4, 1:8, 1:16, respectively). Take 4Fe$_{citrate}$-N-C-3 as an example, it means using ferric citrate as iron source and the 1:16 molar ratio between 2-methylimidazole and metal with 4% Fe, 96% Zn metal moles. In the process of synthesis, 13.136 g (0.16 mmol) 2-methylimidazole was dissolved in 100 mL deionized water (DI) in a flask. Then, 2.8559 g (0.01 mol × 96%) Zinc nitrate hexahydrate ($Zn(NO_3)_2{\cdot}6H_2O$) and 0.09792 g (0.01 mol × 4%) Ferric citrate were dissolved in 100 mL DI in another flask. Two solutions were mixed at a constant temperature of 60 °C for 24 h with continuous stirring. The suspension was obtained by filtering and then washed with DI several times. The yellow power was dried at 60 °C in a vacuum oven.

The final catalysts were prepared through a programmed pyrolysis in the N_2 and NH_3 atmosphere. The precursor was put in the tube furnace and heated to 950 °C at 5 °C/min under a N_2 flow, then secondary NH_3 pyrolysis was applied at 950 °C under a NH_3 flow for 15 min and then kept another 105 min in flowing N_2, cooled downed to room temperature naturally. 4Fe$_{citrate}$-C-3 was prepared with same procedure without secondary NH_3 pyrolysis treatment.

The morphology and size of catalysts were characterized by scanning electron microscopy (SEM, Hitachi S-4700), transmission electron microscopy (TEM, HT 7700) and high-resolution transmission electron (HRTEM, FEI Tecnai G2 F2). The crystal structure information was obtained by X-ray diffraction (XRD) with Cu Kα radiation ($\lambda = 0.154178$ nm) at 2θ ranges from 5° to 90° X-ray photoelectron spectroscopy (XPS) analysis was conducted with ESCALAB 250 (Thermo Fisher Scientific USA) equipped with an A1 Kalph 150 W X-ray source. The Raman spectra was tested with 514 nm laser as the excitation source. Nitrogen adsorption-desorption measurement was performed on a Micromeritics (ASAP 2460). The pore size distribution and specific surface area were measured by Barrett-Joyner-Halenda (BJH) method and Brunauer-Emmett-Teller (BET) method, respectively.

The electrochemical performance of materials was performed on a electrochemical workstation with CHI760E Instrument at room temperature and all tests were carried out under saturated oxygen or nitrogen conditions. We used the traditional three-electrode system to test the oxygen reduction performance of the materials, in which saturated calomel electrode (SCE) as reference electrode, carbon rod as counter electrode and a glass carbon rotating disk electrode coated with catalyst film as working electrode. The electrode potential of oxygen reduction performance described in this paper was converted reversible hydrogen electrode potential (RHE) according to the equation ($E_{RHE} = E_{SCE} + 0.059pH + E^0{}_{SCE}$).

The preparation process of working electrode: synthesized 5 mg catalyst was dispersed in a mixed solution of Nafion solution (100 μL, 0.5 wt%) and anhydrous ethanol (900 μL), then sonicated at least 30 min to form a homogeneous suspension. The 10 μL suspension ink was dropped on the polished glass carbon electrode with 5 mm diameter and dried at room temperature (the catalyst loading is 0.255 mg/cm^2).

Cyclic voltammetry (CV) test was performed in a voltage range from 0 to 1.0 V (*vs.* RHE) at a scan rate of 10 mV/s and the linear sweeping voltammetry (LSV) measurement was performed at a scan rate of 5 mV/s with a rotating rate of 1600 rpm in the same voltage range. Rotating ring-disk electrode (RRDE) measurement was also performed to investigate the electron transfer number and yield of H_2O_2% in the reaction. The Tafel slope can be calculated from the LSV curve data to characterize the oxygen reduction kinetics of the catalyst according to Eq. 1:

$$J_k = \frac{|J_L * J|}{|J_L| - |J|} \tag{1}$$

Meanwhile, electron transfer number is calculated by the Kouteckye-Levich (K-L) equation:

$$\frac{1}{J} = \frac{1}{J_L} + \frac{1}{J_K} = \frac{1}{B\omega^{1/2}} + \frac{1}{J_K} \tag{2}$$

$$B = 0.6nFC_0(D_0)^{2/3}F\nu^{-1/6} \tag{3}$$

The electron transfer number of catalysts and yield of H_2O_2% can be measured by using RRDE with Eqs. 4 and 5:

$$n = 4 \times \frac{I_d}{I_d + \frac{I_r}{N}} \tag{4}$$

$$H_2O_2\% = 200 \times \frac{I_r/N}{I_d + I_r/N} \tag{5}$$

where I_d is disk current, I_r is ring current and N = 0.37 is the current collection efficiency of the Pt ring.

The C_{dl} was calculated from double layer charging curves in non-faradic potential range of 1.00–1.05 V (*vs.* RHE), then electrochemically active surface area (ECSA) was further calculated by the relation between C_{dl} and scan rate (υ) according to Eq. 6:

$$ECSA = \frac{j/\upsilon}{C_{GC}} \tag{6}$$

C_{GC} is double layer capacitance of glassy carbon electrode (0.2 F/m^2).

The durability of catalysts was assessed by *i-t* chronoamperometric measurements at fixed potential in O_2-saturated for 50,000 s. The methanol tolerance of the catalyst was evaluated by the change of current density when 6 mL of methanol was added into electrolyte during the chronoamperometric measurement.

As is shown in Scheme 1, the prepared electrocatalysts were synthesized towards stepwise pyrolysis strategy. ZIF-derived precursors were synthesized by adding ferric salts with diverse anion, *i.e.*, $FeCl_3$, $FeNO_3$, $FeSO_4$ and ferric citrate, in an aqueous solution, various catalysts were obtained after the pyrolysis to explore influence of different anions on the electrocatalytic ORR activity. From Figs. 1a-d, the morphology of catalysts was observed

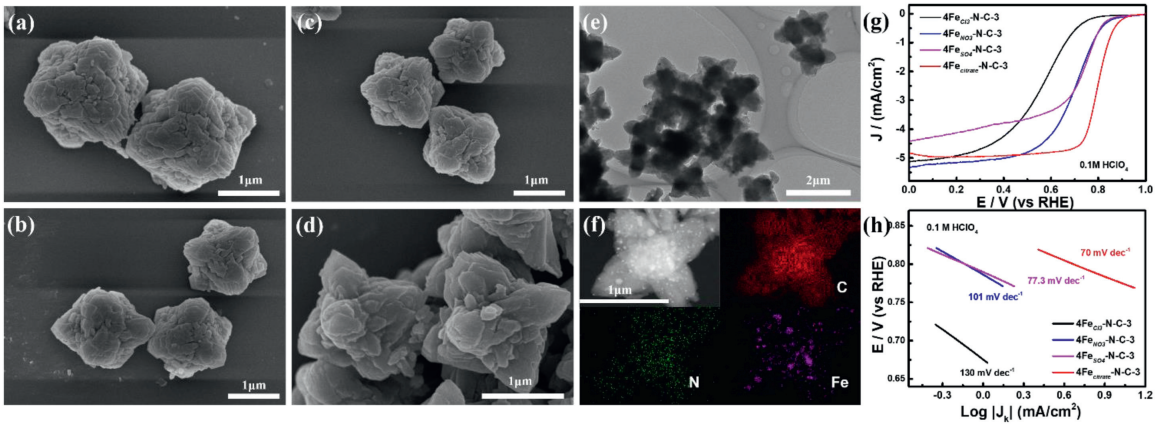

Fig. 1. SEM images of (a) 4Fe$_{Cl3}$-N-C-3, (b) 4Fe$_{NO3}$-N-C-3, (c) 4Fe$_{SO4}$-N-C-3, (d) 4Fe$_{citrate}$-N-C-3. (e) TEM image of 4Fe$_{citrate}$-N-C-3. (f) HRTEM image of 4Fe$_{citrate}$-N-C-3 and corresponding elemental mapping of N, C and Fe. (g) LSV curves of the different iron salt catalysts. (h) Corresponding Tafel plots from RDE polarization curves.

by SEM, which surface is relatively rough. The 4Fe$_{citrate}$-N-C-3 catalyst shows an obvious outward spreading flower-like morphology while the other three catalysts all exhibits block-like structure which presented slight tendency with outward growth. More importantly, compared with Fig. S1 (Supporting information), the results show that 4Fe$_{citrate}$-N-C-3 could maintain the original morphology after calcination.

The 4Fe$_{citrate}$-N-C-3 exhibits a different shape from the other ferric salts, possibly due to the co-effect for coordination of citrate ions with Zn ions and the exchange with partial 2-methylimidazole ligands [26]. The rough surface of the sample indicates that abundant pore structures may have formed during the calcination process. The XRD pattern of precursor (4Fe$_{citrate}$-ZIF8–3) also shows that the addition of coordination effect of ferric citrate affects the crystal structure (Fig. S2c in Supporting information) [28]. The oxygen reduction characteristic of all catalysts is shown in Fig. 1g and the electrocatalytic performance of various anions is significantly different. The half-wave potential of catalysts prepared by different anions are 0.559, 0.697, 0.725 and 0.8 V (*vs.* RHE) in acid media, respectively. The Tafel slope of 4Fe$_{citrate}$-N-C-3 is 70 mV/dec, which is the smallest of all the samples according to Fig. 1h. The results show that it has the best kinetics for oxygen reduction reaction [34]. The use of different iron sources as iron sources has a significant impact on the amount of doped iron into the catalyst, which may affect the site density of the catalyst, and thus affect the related electrochemical performance (Fig. S3 in Supporting information). Therefore, ferric citrate was selected as the iron source for the subsequent material preparation. Furthermore, a small amount of metal particles can be seen from TEM in Fig. 1e. HRTEM images in Figs. S2a and b (Supporting information) also show the formation of related metal nanoparticles and carbon layers with well-defined lattice distance of 0.204 nm and 0.36 nm, which assigned to (119) planes of the Fe_2O_3 phase (PDF#25–1402) and (002) planes of graphite phases (PDF#26–1080), respectively, and it consistent with the characteristic peak (35.6° and 26.6°) in XRD spectrum (Fig. S2d in Supporting information). Notably, some studies has shown that nano-particles coated with carbon layer can effectively improve ORR activity [35]. Meanwhile, the corresponding element mapping confirms that Fe and N elements are uniformly distributed on the carbon after carbonization (Fig. 1f).

In order to analyze the effect of ammonia activation on the structure and composition of the catalyst, under the same condition, 4Fe$_{citrate}$-C-3 was prepared without ammonia treatment, which was characterized by XPS, Raman and BET (Fig. 2). The surface elemental composition of the substance was obtained through XPS. Obviously, the total nitrogen content of 4Fe$_{citrate}$-N-C-3 was significantly increased after ammonia gas activation (Fig. S4 in Supporting information). As shown in Fig. 2c, N 1s peak of 4Fe$_{citrate}$-N-C-3 was deconvolved with pyridinic N (398.6 eV), pyrrolic N (400 eV), graphitic N (401.1 eV) and oxidized N (402.7 eV) [36,37], which accounted for 40.22%, 22.25%, 25.75% and 11.78% (Fig. S5 in Supporting information), respectively. In contrast, 26.8% of pyridinic N, 21.98% of pyrrolic N, 26.21% of graphitic N and 24.92% of oxidized N were presented in 4Fe$_{citrate}$-C-3 (Fig. S5). Recent studies demonstrated that the high content of pyridine nitrogen and graphite nitrogen is more conducive to the formation of active sites and improve the ORR activity [38,39]. Through comparison of N content, we found that the percentage of pyridinic N and graphitic N in the 4Fe$_{citrate}$-N-C-3 is higher (the specific content is shown Fig. S5), which is expected to improve the ORR performance. Fe 2p spectrum of 4Fe$_{citrate}$-N-C-3 (Fig. 2b) and 4Fe$_{citrate}$-C-3 (Fig. 2d) was deconvolved several pairs of peaks, the peaks at 709.2 eV and 711.5 eV can be assigned to $2p_{3/2}$ of Fe^{2+} and Fe^{3+} species, respectively. The peaks at 723.8 and 726 eV can be attributed to $2p_{1/2}$ of Fe^{2+} and Fe^{3+} species and the other peak at 719.5 eV is attributed to a satellite peak [36,40]. Meanwhile, Fig. S4 shows that 4Fe$_{citrate}$-N-C-3 has the higher Fe content (0.58%) than 4Fe$_{citrate}$-C-3, probably because the increase of nitrogen content will anchor more Fe element, which is beneficial to the formation of effective active sites [41,42]. It can be seen from Raman spectra in the Fig. 2e that 4Fe$_{citrate}$-N-C-3 has a higher I_D/I_G value (1.049), which indicates NH_3 pyrolysis treatment increased the defects and disorder in the structure of catalyst so as to better expose the active site and further improve the catalytic performance of ORR [41]. The nitrogen adsorption-desorption isotherms were tested to get the information of BET specific surface area and porous size distribution. 4Fe$_{citrate}$-N-C-3 has the larger specific surface area, which was measured as 776 m^2/g by N_2 adsorption-desorption isotherms displayed in Fig. 2f (S_{BET} of 4Fe$_{citrate}$-C-3 is 695 m^2/g). The pore size distribution curves indicates that micropores of 4Fe$_{citrate}$-N-C-3 increased and some expand to become mesopores during ammonia activation, forming the hierarchical pore structure (Fig. S6 in Supporting information) [43], which facilitates the exposure of active sites and mass transfer during the reaction [44].

To explore the effect of catalysts on ORR catalytic performance with diverse compositions, catalysts with several ratios between metal and 2-methylimidazol and Fe-doping content were prepared. Firstly, the molar ratio between metal and 2-methylimidazole varies from 1:4, 1:8 and 1:16, respectively, then 2Fe$_{citrate}$-N-C-1, 2Fe$_{citrate}$-N-C-2 and 2Fe$_{citrate}$-N-C-3 were obtained after calcination pyrolysis. Different proportions of 2-methylimidazol affected the morphology of the electrocatalysts as can be seen from the SEM

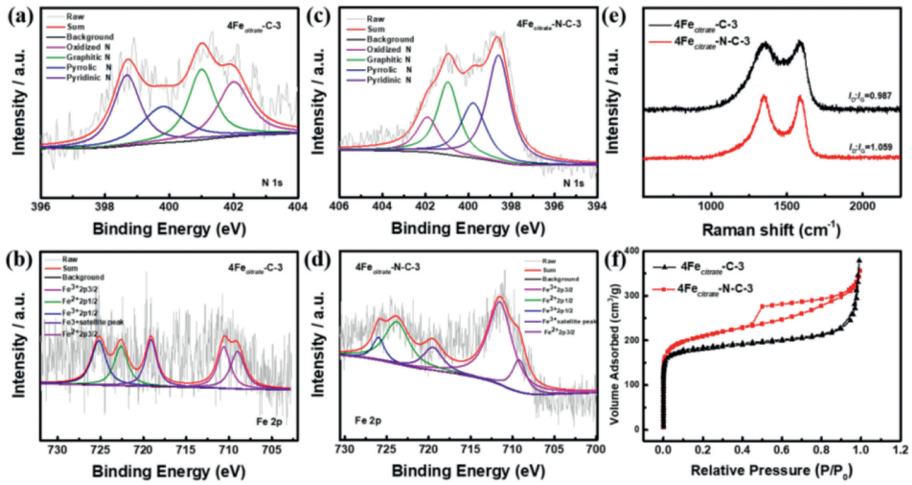

Fig. 2. (a) High-resolution N 1s spectrum of 4Fe$_{citrate}$-C-3. (b) High-resolution Fe 2p spectrum of 4Fe$_{citrate}$-C-3. (c) High-resolution N 1 s spectrum of 4Fe$_{citrate}$-N-C-3. (d) High-resolution Fe 2p spectrum of 4Fe$_{citrate}$-N-C-3. (e) Raman spectra of 4Fe$_{citrate}$-C-3 and 4Fe$_{citrate}$-N-C-3. (f) N_2 isotherms of 4Fe$_{citrate}$-C-3 and 4Fe$_{citrate}$-N-C-3.

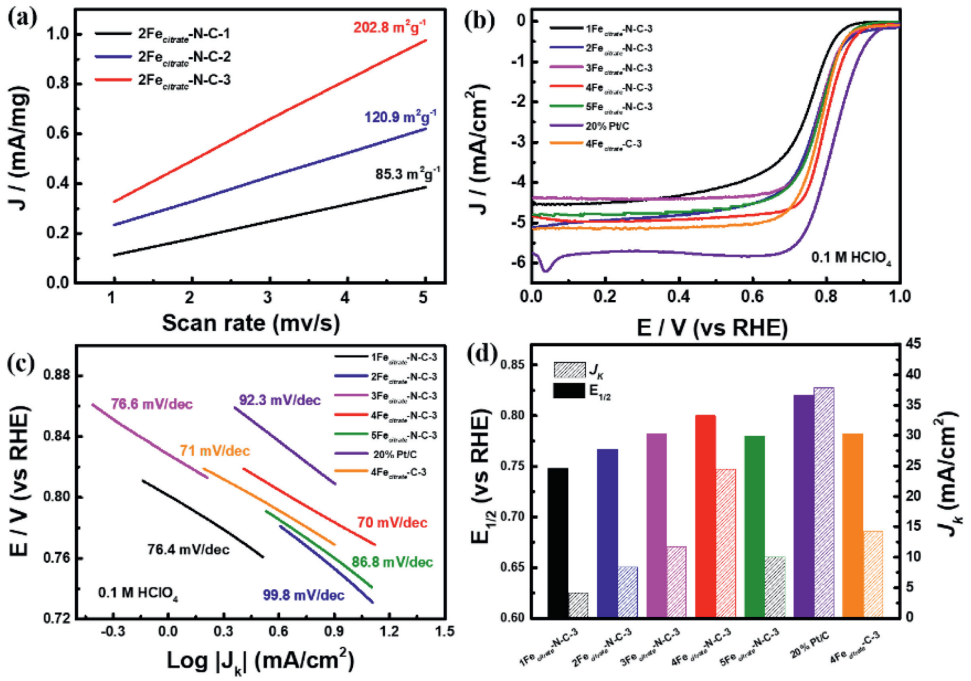

Fig. 3. (a) Corresponding ECSA of different 2-methylimidazol ratios from RDE polarization curves. (b) LSV curves of different Fe doping samples; (c) Corresponding Tafel plots from RDE polarization curves. (d) Corresponding J_k (left) and half-wave potential (right). All the catalysts tested in O_2-saturated in 0.1 mol/L $HClO_4$ solutions.

and TEM images in Fig. S7 (Supporting information). Furthermore, a higher I_D/I_G value (1.03) of 2Fe$_{citrate}$-N-C-3 was obtained by Raman spectrum (Fig. S8 in Supporting information), which may be caused by its particular morphological structure due to the ligand molar ratio. It can be speculated that the flower-like morphology enhances the disorder of the structure, which can expose more active sites. The results also supported by the data of electrochemical active surface area (ECSA) electrochemical test and corresponding LSV curves, in which 2Fe$_{citrate}$-N-C-3 with flower-like structure exhibits a larger ECSA (202 m^2/g) (Fig. 3a) and higher $E_{1/2}$ (0.767 V) (Fig. S9 in Supporting information). That can be indicated that the extended morphology and abundant pore structure can effectively expose the active area and improve the ORR activity in the reaction process.

As is shown in Fig. 3b, the effect of doped Fe amount is also investigated by gradually increasing the amount of iron doping [45]. Among all samples, 4Fe$_{citrate}$-N-C-3 shows the best oxygen reduction performance in both 0.1 mol/L KOH and 0.1 mol/L $HClO_4$ media, which indicates that the 4% Fe-doping is optimal content. Specifically, 4Fe$_{citrate}$-N-C-3 has the most positive half-wave potential ($E_{1/2}$) of 0.9 V (*vs.* RHE) in alkaline electrolyte, which is higher than other Fe doping content and 4Fe$_{citrate}$-C-3 (0.882 V), and even exceeds that of commercial Pt/C (0.87 V). Similarly, 4Fe$_{citrate}$-N-C-3 has the encouraging ORR performance with a half-wave potential ($E_{1/2}$) of 0.8 V (*vs.* RHE), which is close to commercial Pt/C (0.82 V) and higher than 4Fe$_{citrate}$-C-3 (0.783 V) in 0.1 mol/L $HClO_4$ electrolyte (Fig. 3b). With the increase of Fe molar ratios from 0.01 to 0.04, the half-wave potential gradually increased and reached the peak at 0.04 Fe doping, which is consistent with the trend of dynamic current (J_k) in Fig. 3d. It should be related to the number of active sites in the catalyst, which is well evidenced by the Fe content measured by the inductively coupled plasma optical emission spectroscopy (ICP-OES) in Fig. S11 (Supporting information). Furthermore, the excellent ORR activity for synthesized materials

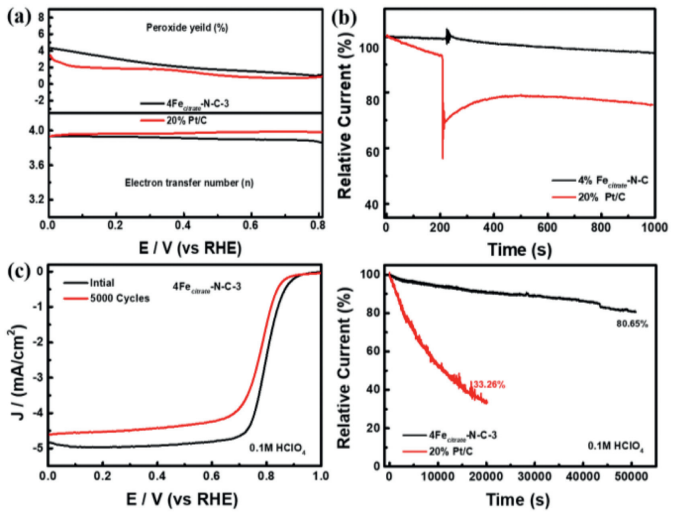

Fig. 4. (a) Electron transfer number and H_2O_2 yield of 4Fe$_{citrate}$-N-C-3 and Pt/C measured by RRDE. (b) The chronoamperometric responses of 4Fe$_{citrate}$-N-C-3 and Pt/C at 0.55 V (*vs.* RHE) with addition of 6 mL methanol. (c) Polarization curves for 4Fe$_{citrate}$-N-C-3 before and after 5000 cycles in an O_2-saturated 0.1 mol/L $HClO_4$ solution. (d) Normalized *i-t* cures at 0.55 V (*vs.* RHE) of 4Fe$_{citrate}$-N-C-3 and Pt/C.

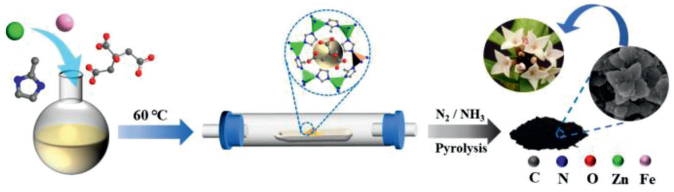

Scheme 1. A schematic illustration of the synthetic process of catalyst.

were further confirmed by the Tafel slope. As displayed in Fig. 3c, 4Fe$_{citrate}$-N-C-3 has the lowest Tafel slope of 70 mV/dec, which is better than that of other catalysts, representing faster ORR kinetics of 4Fe$_{citrate}$-N-C-3 for the ORR.

Based on the fact that 4Fe$_{citrate}$-N-C-3 showed the best electrochemical ORR activity and reaction kinetics, the other ORR performance tests using 4Fe$_{citrate}$-N-C-3 as the best sample were performed. The electron transfer number (*n*) and yield of hydrogen peroxide (H_2O_2) were measured by using RRDE. In the voltage range of 0–0.8 V (*vs.* RHE), the electron transfer number basically maintained between 3.9 and 4.0, which is very close to the theoretical value of commercial 20 wt% Pt/C (Fig. 4a). Additionally, LSV tests at different rotating speeds were carried out, and the electron transfer number calculated by *K-L* (Kouteckye-Levich) equation was about 4, which was consistent with the results of RRDE test (Fig. S12 in Supporting information). The yield of H_2O_2 remains below 5%, indicating that the four-electron pathway is more inclined to react in the reaction process, which the reaction product is water without any pollution to the environment. The commercial Pt/C appeared a significant current density drop instantly in Fig. 4b, while 4Fe$_{citrate}$-N-C-3 was not greatly affected and remained stable when 6 mL methanol was added to the electrolyte at 200 s in the chronoamperometry curve (*i-t*) test mode. 4Fe$_{citrate}$-N-C-3 has a good methanol resistance and could be used as a potential methanol fuel catalyst.

Except for excellent ORR performance, the durability is also another significant parameter for practical application [46]. Thus, two methods were used to evaluate the stability of the electrocatalyst in this work. The first method was investigated to cycle CV curve over a voltage range of 0.6–1.0 V (*vs.* RHE) at rate of 100 mV/s, the half-wave potential was only poor 20 mV than initial $E_{1/2}$ after 5000 cycles (Fig. 4c). At the same time, through the chronoamperometric test to accelerate aging process, 4Fe$_{citrate}$-N-C-3 still maintain more than 80% of original current activity after 50,000 s, while the commercial Pt/C decreased significantly to 33% after 20,000 s under the same test condition in Fig. 4d. The results obviously revealed that 4Fe$_{citrate}$-N-C-3 has better stability than commercial Pt/C. The unique flower-like morphology with ferric citrate doping and effective NH_3 heat treatment for catalyst provide the higher surface area and more exposed active sites, which makes that 4Fe$_{citrate}$-N-C-3 is a potential electrode catalyst for proton exchange membrane fuel cell in acidic medium.

In summary, we synthesized ferric citrate doped Fe-N-C electrocatalyst with flower-like morphology through a stepwise pyrolysis method. The ammonia activation during pyrolysis was used to increase the nitrogen species and enrich the pore structure, which effectively increasing the number of effective active sites and the accessible active area. By controlling the proportion and composition of the precursor, the catalyst of 4Fe$_{citrate}$-N-C-3 with the best ORR performance was synthesized when the 2-methylimidazol ratio of 1:16 and the iron doping is 4%. The half-wave potential reaches 0.8 V and 0.9 V (*vs.* RHE) in acid and alkaline, respectively. More importantly, it exhibits excellent stability and methanol tolerance. This work provides a good reference for the development of low cost and high performance non-noble metal oxygen reduction catalysts.

Declaration of competing interest

The authors declare that they have no known competing financial interests or personal relationships that could have appeared to influence the work reported in this paper.

Acknowledgments

This work was supported by the National Key Research and Development Program of China (No. 2019YFA0210300), the Natural Science Foundation of China (Nos. 21922802, 52074119); the Beijing Natural Science Foundation (No. JQ19007), the Joint Funds of the National Natural Science Foundation of China (No. U20A20280), Talent cultivation of State Key Laboratory of Organic-Inorganic Composites, "Double-First-Class" construction projects (Nos. XK180301, XK1804–02), Distinguished Scientist Program at BUCT (No. buctylkxj02).

Supplementary materials

Supplementary material associated with this article can be found, in the online version, at doi:10.1016/j.cclet.2021.06.054.

References

[1] S. Chu, A. Majumdar, Nature 488 (2012) 294–303.
[2] S.T. Thompson, A.R. Wilson, P. Zelenay, et al., Solid State Ion. 319 (2018) 68–76.
[3] M. Shao, Q. Chang, J.P. Dodelet, R. Chenitz, Chem. Rev. 116 (2016) 3594–3657.
[4] X. Huang, T. Shen, T. Zhang, et al., Adv. Energy Mater. 10 (2020) 1900375.
[5] A. Zubiaur, N. Job, Appl. Catal. B: Environ. 225 (2018) 364–378.
[6] G. Wu, Front. Energy 11 (2017) 286–298.
[7] X. Wang, Z. Li, Y. Qu, et al., Chem 5 (2019) 1486–1511.
[8] B. Garlyyev, K. Kratzl, M. Rück, et al., Angew. Chem. Int. Ed. 58 (2019) 9596–9600.
[9] Y. Xiong, Y. Ma, L. Zou, et al., J. Catal. 382 (2020) 247–255.
[10] P.P. Lopes, D. Li, H. Lv, et al., Nat. Mater. 19 (2020) 1207–1214.
[11] L. Du, L. Xing, G. Zhang, S. Sun, Carbon 156 (2020) 77–92.
[12] B. Sidhureddy, S. Prins, J. Wen, et al., ACS Appl. Mater. Interfaces 11 (2019) 18295–18304.
[13] Y. Wang, C. Wöll, Catal. Lett. 148 (2018) 2201–2222.
[14] Q. Liu, X. Liu, L. Zheng, J. Shui, Angew. Chem. Int. Ed. 57 (2018) 1204–1208.
[15] S.H. Lee, J. Kim, D.Y. Chung, et al., J. Am. Chem. Soc. 141 (2019) 2035–2045.
[16] D. Liu, J.C. Li, S. Ding, et al., Small Methods 4 (2020) 1900827.
[17] G. Chen, P. Liu, Z. Liao, et al., Adv. Mater. 32 (2020) 1907399.
[18] Y. Zhao, M. Zhang, X. Wen, Z. Xiang, Green Chem. Eng. 1 (2020) 63–69.

[19] C.C. Hou, L. Zou, L. Sun, et al., Angew. Chem. Int. Ed. 59 (2020) 7384–7389.
[20] W. Zhang, H. Sun, Z. Zhu, et al., Renew. Energy 146 (2020) 2270–2280.
[21] X. Wan, X. Liu, Y. Li, et al., Nat. Catal. 2 (2019) 259–268.
[22] J. Lilloja, E. Kibena-Põldsepp, A. Sarapuu, et al., ACS Catal. 11 (2021) 1920–1931.
[23] H. Liu, S. Wang, L. Long, J. Jia, M. Liu, Nanotechnology 32 (2021) 205402.
[24] X. Chen, X. Zhen, H. Gong, et al., Chin. Chem. Lett. 30 (2019) 681–685.
[25] Q. Wang, Y. Yang, F. Sun, et al., Adv. Energy Mater. (2021) 2100219.
[26] Y. Ye, F. Cai, H. Li, et al., Nano Energy 38 (2017) 281–289.
[27] R.M. Cigala, F. Crea, C. De Stefano, et al., Monatshefte für Chem. Chem. Mon. 146 (2015) 527–540.
[28] W. Li, W. Ding, Y. Nie, Q. He, J. Jiang, Z. Wei, ACS Appl. Mater. Interfaces 11 (2019) 22290–22296.
[29] R. Wang, P. Zhang, Y. Wang, et al., Prog. Nat. Sci. Mater. Int. 30 (2020) 855–860.
[30] Y. Gong, H. Fei, X. Zou, et al., Chem. Mater. 27 (2015) 1181–1186.
[31] X. Wang, J.S. Lee, Q. Zhu, J. Liu, Y. Wang, S. Dai, Chem. Mater. 22 (2010) 2178–2180.
[32] Y. Wang, X. Chen, Q. Lin, et al., Nanoscale 9 (2017) 862–868.
[33] Q. Niu, J. Guo, B. Chen, et al., Carbon 114 (2017) 250–260.
[34] L. Jin, H. Pang, Chin. Chem. Lett. 31 (2020) 2300–2304.
[35] L. Yu, D. Deng, X. Bao, Angew. Chem. Int. Ed. 59 (2020) 15294–15297.
[36] M. Sun, D. Davenport, H. Liu, et al., J. Mater. Chem. A 6 (2018) 2527–2539.
[37] J. Wang, W. Liu, G. Luo, et al., Energy Environ. Sci. 11 (2018) 3375–3379.
[38] D. Guo, R. Shibuya, C. Akiba, et al., Science 351 (2016) 361.
[39] H. Zhu, Z. Sun, N. Chen, et al., ChemElectroChem 4 (2017) 1117–1123.
[40] X. Xie, L. Shang, R. Shi, et al., Nanoscale 12 (2020) 13129–13136.
[41] X. Fu, N. Li, B. Ren, et al., Adv. Energy Mater. 9 (2019) 1803737.
[42] U.I. Kramm, J. Herranz, N. Larouche, et al., PCCP 14 (2012) 11673–11688.
[43] M. Wu, K. Wang, M. Yi, et al., ACS Catal. 7 (2017) 6082–6088.
[44] X. Xu, Z. Xia, X. Zhang, et al., Nanoscale 12 (2020) 3418–3423.
[45] F. Xiao, G.L. Xu, C.J. Sun, et al., Nano Energy 61 (2019) 60–68.
[46] J. Gu, Y. Xu, Q. Li, H. Pang, Chin. Chem. Lett. 32 (2021) 2017–2020.